Hierarchical Design Enables Sufficient Activated CO_2 for Efficient Electrolysis of Bicarbonate to CO

Mengxin Shen[1,4], Liyao Ji[1,4], Dongfang Cheng[3,4], Qinwen Xue[1], Shijia Feng[1], Yao Luo[1], Shuying Chen[1], Ziwei Wang[1], Jiahao Wang[1], Hongzhi Zheng[1], Xiaojun Wang[1,2*], Philippe Sautet[3], Jia Zhu[1,2*]

[1]National Laboratory of Solid State Microstructures, College of Engineering and Applied Sciences, Jiangsu Key Laboratory of Artificial Functional Materials, Collaborative Innovation Center of Advanced Microstructures, Frontiers Science Center for Critical Earth Material Cycling, Nanjing University, Nanjing 210093, P.R. China

[2]School of Sustainable Energy and Resources, Nanjing University, Suzhou 215163, P.R. China

[3]Department of Chemical and Biomolecular Engineering, University of California, Los Angeles, Los Angeles, California 90095, United States

[4] These authors contributed equally to this work.

*Correspondence: jiazhu@nju.edu.cn, xiaojunwang@nju.edu.cn

SUMMARY

Bicarbonate electrolyzers (BCEs) offer a promising approach to reducing the energy cost of CO_2 reduction by integrating upstream carbon capture and downstream electrochemical utilization. However, the faradaic efficiency of CO_2 electrolysis in BCEs has been limited by insufficient activated CO_2 on the catalyst surface. We report a hierarchical design strategy combining molecular and system-level innovations to ensure sufficient activated CO_2 on the catalyst in BCEs. At the molecular scale, we introduce a single-atom catalyst CoPc@CNT with strong CO_2 adsorption to prevent CO_2 desorption from the catalyst surface. Systemically, a cathodic electrolyte cross-flow strategy further enhances CO_2 mass transfer. This approach achieves a faradaic efficiency exceeding 96.2% for CO at 50-300 mA cm^{-2}, with a 36.0% and 35.3% reduction in overall energy cost compared to conventional BCEs and CO_2 gas-fed electrolyzers, respectively. This innovative strategy represents a significant advancement of low-energy consumption exhaust conversion technologies for carbon neutrality.

INTRODUCTION

Electrochemical CO_2 reduction reaction (CO_2RR)[1] typically requires high-purity and high-pressure gaseous CO_2 as the raw material whose attainment includes energy-intensive steps such as CO_2 release and compression (**Fig. S1**).[2-4] A promising alternative is directly using bicarbonate electrolyzers (BCEs) to integrate CO_2 capture and electrochemical reduction and to avoid the energy-intensive steps.[2,3,5-7]

According to the techno-economic analysis, the commercialization of the CO_2 electrolysis system needs to ensure the yield and economics of products, requiring a current density greater than 200 mA cm^{-2} and a FE of approximately 90% at operating voltages lower than 3.0 V.[8-10] In pursuit of these targets for BCEs, significant efforts[11,12] have been devoted to improving the faradaic efficiency of CO (FE_{CO}) at industrially relevant current densities. Various innovative approaches to promote CO_2 mass transfer have been applied such as screening CO_2-capture medium,[13-18] optimizing electrode hydrophobicity,[3,19,20], and changing the fluid flow pattern.[3] Despite these advancements, which have elevated FE_{CO} from 20% to 60% at 200 mA cm^{-2}, BCEs have yet to fulfill the criteria for industrial applicability.[8-10]

Achieving a significant enhancement in faradaic efficiency necessitates a detailed mechanistic insight into the primary limitations. In the context of BCEs for CO_2RR, the supply of CO_2 is markedly lower than that in traditional gas-fed electrolyzers (**Fig. S2**). This difference arises because, in BCEs, CO_2 generation hinges on the reaction between bicarbonate ions (HCO_3^-) and protons (H^+) within the bulk electrolyte (**Eq. S1 and Eq. S2**).[21] Subsequently, the insufficient CO_2 is transferred to the catalyst surface, where its adsorption and activation occur, facilitating the following conversion process (**Fig. S3**).[22-24] Up until now, efforts to boost the faradaic efficiency in BCEs have primarily focused on improving CO_2 mass transfer rates. Yet, there has been rare attention paid to investigating how catalyst-related mechanisms can influence this process. This gap highlights the critical need for further exploration into how enhancing catalyst efficiency and selectivity could significantly impact the overall performance of BCEs.

One of the greatest challenges impeding the faradaic efficiency of CO_2RR in BCEs is to achieve an efficient CO_2 activation process, especially at low CO_2 concentrations. Enhancing the binding ability of the catalyst site towards CO_2 could avoid CO_2 desorption from the catalyst surface and inhibit the hydrogen evolution reaction (HER), which is of great significance for improving faradaic efficiency.[25]

Currently, although the bulk Ag catalyst is widely used in CO_2 gas-fed electrolyzers with FE_{CO} exceeding 90%,[8,26] it exhibits significantly diminished efficiency in BCEs due to their inadequate CO_2 adsorption strength, particularly evident at low CO_2 concentrations where FE_{CO} drops below 60% at 200 mA cm^{-2} under ambient conditions (**Fig. 1a**).[3,21] This stark contrast underscores the need for catalyst optimization in BCEs to address the unique challenges posed by reduced CO_2 availability.

Therefore, there is a need for a strategy that tailors the adsorption energy of the catalyst for CO_2 to achieve highly efficient conversion in direct capture medium electrolysis. Additionally, the limited CO_2 mass transfer leads to less collision between CO_2 and the catalyst surface, also resulting in insufficient activated CO_2 on the catalyst surface.[27] In conventional BCEs, OH^- is generated at the cathode along with the CO_2RR process (**Eq. S1-S3**). Driven by electric field forces, the OH^- aggregates near the surface of the cathodic catalyst act as a CO_2-consuming layer that barriers CO_2 release and transport to the catalyst surface (**Eq. S4 and Eq. S5**) (**Fig. 1a**). Therefore, to improve the faradaic efficiency of CO_2 conversion in BCEs, strategies should be adopted to enhance the catalyst's binding ability to CO_2 and promote CO_2 mass transfer, ultimately increasing the amount of activated CO_2 on the catalyst surface.

Herein, we report a hierarchical strategy integrating molecular-level and system-level designs to ensure sufficient activated CO_2 on the catalyst for the BCEs system (**Fig. 1b**). On the molecular level, the single-atom catalyst (CoPc@CNT) with strong CO_2 binding ability promotes CO_2 activation and conversion. On the system level, our BCEs device adopts a cathodic electrolyte cross-flow strategy. This design channels HCO_3^- directly to the membrane surface through two distinct flow paths to generate CO_2, significantly enhancing mass transfer compared to conventional BCEs reliant on HCO_3^- diffusion. Meanwhile, the cathodic electrolyte vertically passes across the cathodic electrode which not only eliminates the CO_2-consuming layer on the catalyst surface but further promotes CO_2 mass transfer as well. This innovative BCEs system achieves an impressive FE_{CO} of over 96.2% from 50 to 300 mA cm^{-2}. Remarkably, the significantly improved FE_{CO} makes BCEs highly competitive in terms of CO_2 conversion overall energy consumption, 36.0% and 35.3% lower compared to conventional BCEs and CO_2 gas-fed electrolyzers,[2,14,18] respectively.

RESULTS

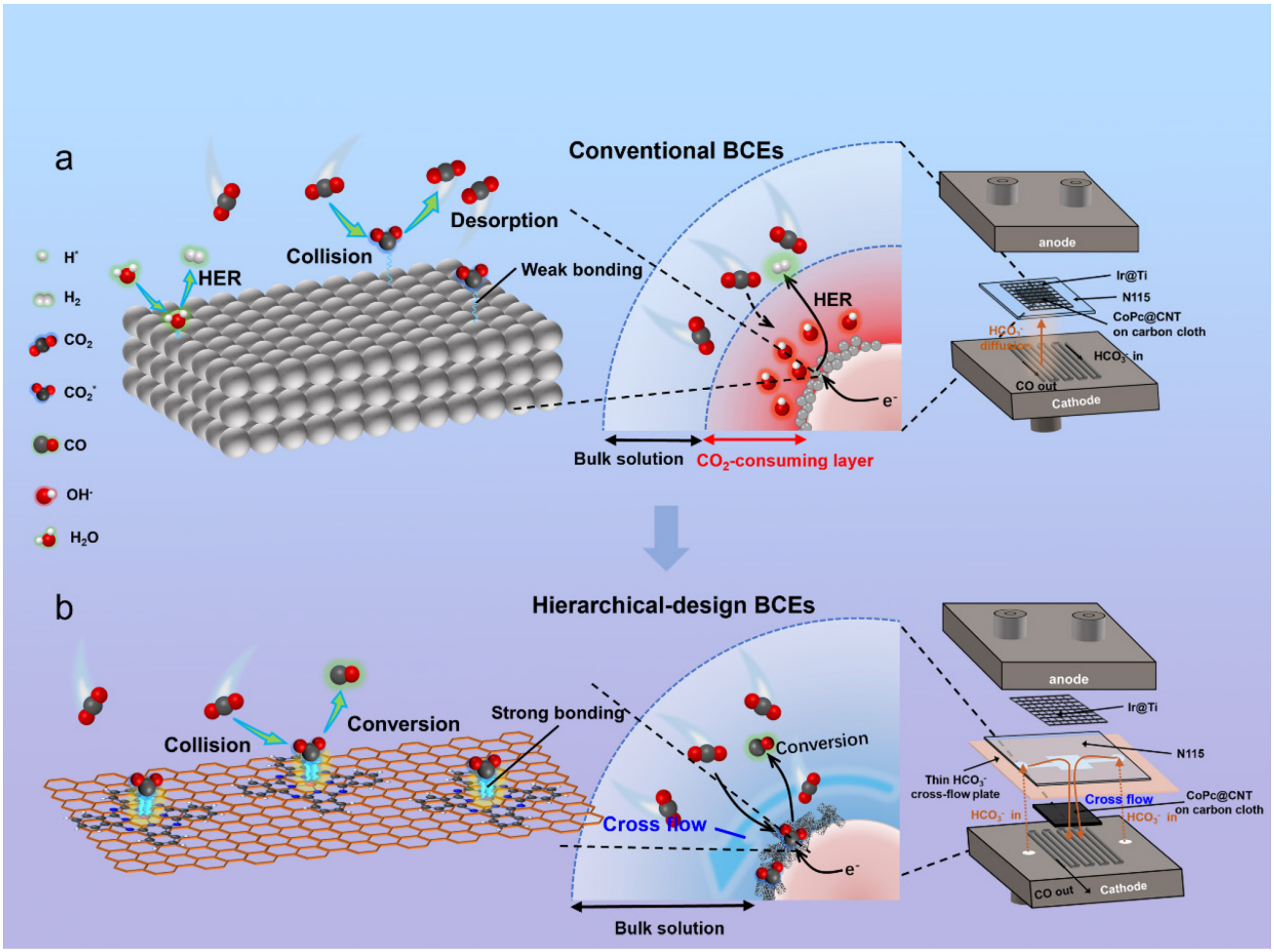

Figure 1: Hierarchical design enables sufficient activated CO_2 for efficient electrolysis of CO_2 to CO in BCEs.

a) In conventional BCEs, conventional Ag catalysts with weak adsorption capability to CO_2 cause the insufficient activation of CO_2. At the same time the OH^- covers the catalyst surface and forms a CO_2-consuming layer, which impedes the CO_2 mass transfer to the catalyst. **b**) In hierarchically designed BCEs, a single-atom catalyst CoPc@CNT with strong CO_2 adsorption capability is introduced to enhance the catalyst binding ability to CO_2 and to facilitate CO_2 activation and conversion. Meanwhile, a strategy of cathodic electrolyte cross-flow is implemented to promote HCO_3^- mass transfer to eliminate the CO_2-consuming layer that developed on the cathodic catalyst surface to further promote CO_2 mass transfer.

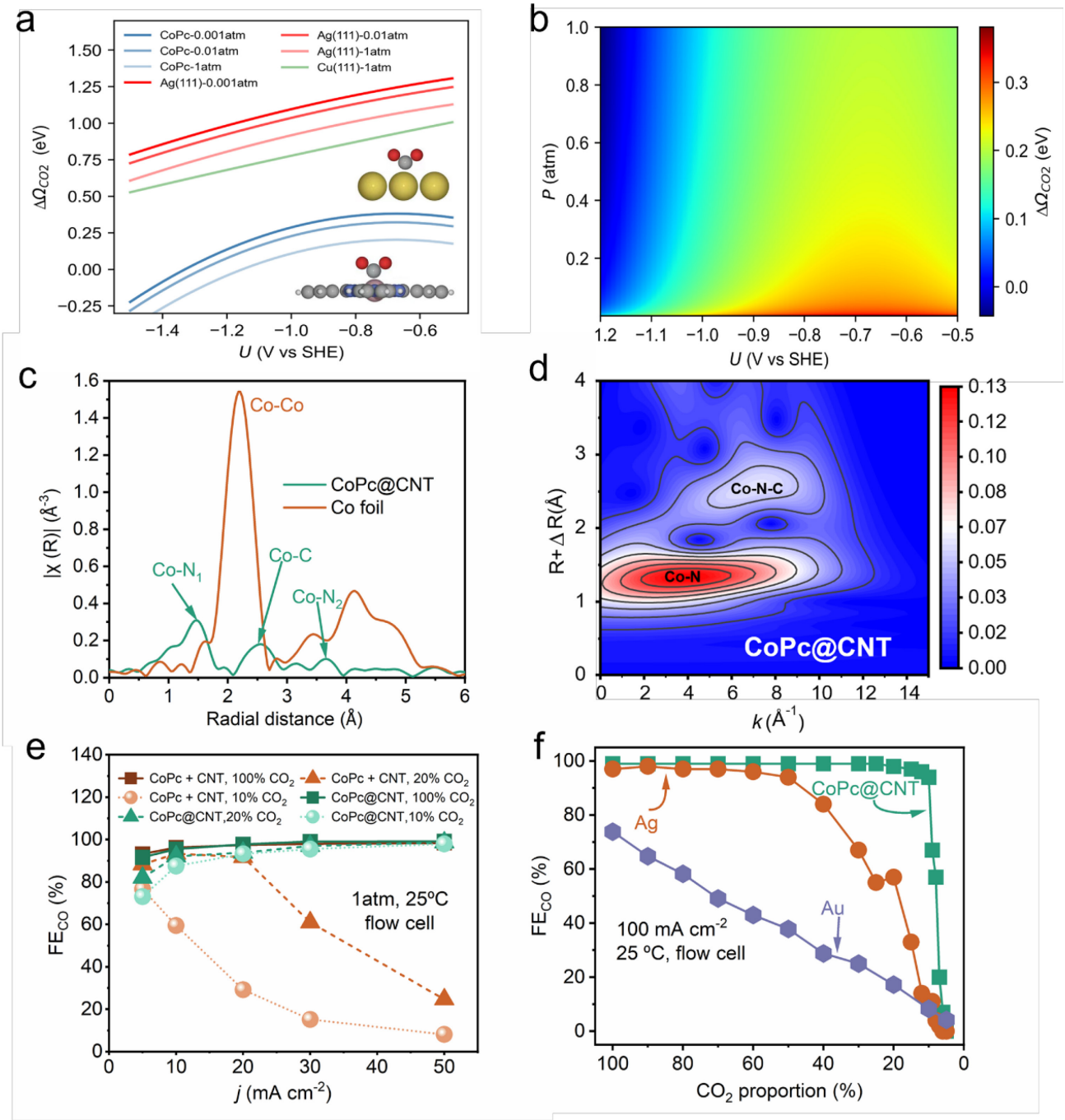

Figure 2: Enhanced CO_2 adsorption by a single-atom-catalyst strategy (CoPc@CNT) enables excellent catalytic performance in low CO_2 concentrations environment.

a) Comparative analysis of CO_2 adsorption energies between CoPc@CNT, Ag, and Cu, as a function of potential under different CO_2 partial pressures. **b**) Investigation of the adsorption energy of CO_2 on CoPc@CNT, considering CO_2 partial pressure and electrode potential. **c**) Co K-edge EXAFS spectra of CoPc@CNT and Co Foil. **d**) Wavelet transform analysis of EXAFS spectra of CoPc@CNT **e**) Evaluation of the performance of CoPc@CNT catalysts without CoPc clusters and CoPc+CNT (two

powders physically mixed in a 1 to 1 ratio by mass without a single-atom dispersion process) catalysts with CoPc clusters at low CO_2 concentrations in a CO_2 gas-fed flow cell. **f**) CO_2RR performance comparison between CoPc@CNT, Ag, and Au at various CO_2 concentrations in a CO_2 gas-fed flow cell, maintaining a constant current density of 100 mA cm^{-2}.

Molecular Level Strategy for Enhancing CO_2 Adsorption

Catalysts with stronger interactions with CO_2 facilitate CO_2 activation and thereby improve the electrocatalytic CO_2RR activity even at low CO_2 concentrations.[28] At present, Ag-based catalysts are usually used as cathode catalysts in BCEs.[3,19,21] However, the low CO_2 affinity on Ag catalysts limits the CO_2RR activity. Transition-metal single-atom catalysts (SACs) generally show stronger CO_2 adsorption compared to bulk catalysts.[27,29] As the transition metal atoms become atomically isolated, there is a concomitant upward shift of the d-band center. This shift results in a decreased density of electrons in the antibonding state, which stabilizes the intermediates.[30] Here, carbon nanotube-loaded cobalt phthalocyanine (CoPc@CNT) (**Fig. S4**) is chosen as a representative single-atom catalyst, which may possess stronger CO_2 adsorption capability. Although these single-atom catalysts have been demonstrated with excellent performance in CO_2 gas-fed electrolyzers,[31-35] their research in BCEs and the relationship between CO_2 adsorption capability and the BCEs performance are still blank.

We first performed grand canonical density functional theory (GCDFT) calculations to compare the potential dependent CO_2 adsorption free energy on the CoPc@CNT catalyst and commonly used Ag and Cu catalyst in CO_2RR. Under a CO_2 pressure of 1 atm, it is clear that the adsorption energy of $*CO_2$ on CoPc@CNT is considerably lower, than that on Ag or Cu, and the difference is more than 0.5 eV in a wide range of potential. It indicates stronger adsorption of CO_2 by CoPc@CNT when CO_2 is under high concentrations (**Fig. 2a**). The adsorption energy of all three catalysts, CoPc@CNT, Ag, and Cu, increases as the CO_2 concentration decreases (from 1 atm to 0.1 atm, further to 0.01 atm). Notably, under low CO_2 partial pressures (0.01 atm, 0.001 atm), the adsorption of $*CO_2$ on Ag proves to be exceptionally difficult, with reaction energy exceeding 0.75 eV on Ag (111) even at substantially negative potentials. This suggests that CO_2RR through bicarbonate reduction will be particularly challenging to achieve. While the $*CO_2$ adsorption on CoPc@CNT at low CO_2 pressure is still considerably stronger than that on Ag at 1 atm, demonstrating the superior CO_2 adsorption capability

of CoPc@CNT. In addition, although CO_2 can be significantly stabilized at the CoPc site, the stabilization effect for CO is not as pronounced. This difference is attributed to the unique ability of the single atom site to stabilize intermediates with large dipole moments as bent CO_2. In contrast, *COOH and *CO exhibit much smaller dipole moments, making them less responsive to single-atom site stabilization, a phenomenon detailed in Chan's study.[36] Consequently, the adsorption energy of CO on CoPc is relatively weak, facilitating its easy desorption, as shown in **Fig. S5**.

As illustrated in **Fig. 2b**, The $*CO_2$ adsorption free energy on CoPc@CNT is highly dependent on the electrode potential and CO_2 pressure. With the applied voltage being more negative and the CO_2 partial pressure increasing, there is a general enhancement in adsorption capability. This phenomenon can be partially attributed to the substantial dipole moment of bent $*CO_2$, which renders it highly responsive to changes in the interfacial electric field, thereby elucidating the strengthened adsorption observed under negative potential conditions. Furthermore, it is noteworthy that pressure exerts a profound influence on the translational entropy of gaseous CO_2. The adsorption process imposes constraints on both the translational and rotational components of the gas's entropy, contributing to the observed enhancement in adsorption energy as pressure undergoes variations. In addition, our previous study[25] showed that the Co single-atom site exhibits a much more energy-localized 3*d* state compared to the dispersed *d* band states for Ag, which is believed to strengthen the interaction between the adsorbate and the metal according to the Newns–Anderson–Grimley model. These DFT findings indicate that CoPc has a strong adsorption capability at low CO_2 concentrations, which makes it an excellent candidate for bicarbonate conversion in BCEs.

The CoPc@CNT was synthesized and characterized to guarantee uniform distribution of Co single-atomic sites on the CNT. A facile method was utilized by mixing the CNT into nearly saturated CoPc solutions with the assistance of magnetic stirring (**Fig. S6**). The X-ray absorption near-edge structure (XANES) spectra (**Fig. S7**) and extended X-ray absorption fine structure (EXAFS) spectra (**Fig. 2c**) show that the oxidation state of the Co atoms in hybrids was approximately +2 and no Co-Co coordination is found, suggesting that CoPc was uniformly anchored onto the CNTs surface at the single molecular level. Comparing wavelet transform analysis of EXAFS spectra of CoPc@CNT with that of CoO or Co foil, only Co-N and Co-N-C bonds are present in CoPc@CNT, which indicates a

mono-dispersion of CoPc at CNTs (**Fig. 2d and Fig. S8**). Scanning electron microscopy (SEM) images also indicate that no CoPc clusters are present in CoPc@CNT, whereas rod-like CoPc clusters are observed in CoPc+CNT (**Fig. S9**). TEM images and corresponding EDS elemental maps of CoPc@CNT indicate N and Co elements' uniform dispersion at CNTs (**Fig. S10**). XRD patterns and Raman spectra are further used to characterize the CoPc@CNT and CoPc+CNT (**Fig. S11**), and it shows similar signature vibrational peaks and crystal structure of CoPc+CNT and CoPc. It is noted that some of the CoPc vibrational features are not observed with CoPc@CNT, suggesting strong CoPc-CNT electronic interactions that prohibit some of the vibrational modes of the CoPc molecules on CNT. After 3600 s of reaction in cross-flow BCEs at a flow rate of 240 ml min^{-1} and a current density of 100 mA cm^{-2}, the XRD pattern as well as Raman spectra of CoPc@CNT show that the reaction process did not change the distribution state of CoPc on CNT.

To verify the high CO_2 adsorption capability of CoPc@CNT at low CO_2 concentration, and to demonstrate the necessity of single-atom dispersion, we tested the CO_2RR electrochemical performance of CoPc@CNT in a CO_2 gas-fed flow cell under varying CO_2 partial pressure mixing CO_2 with Ar in a different ratio and compared it with CoPc+CNT and bulk Ag catalyst. At a 100% CO_2 concentration, both the CoPc@CNT and CoPc+CNT show a similar FE_{CO} over 90% from 10 to 50 mA cm^{-2} (**Fig. 2e**). However, there is a significant difference in their performance when the CO_2 concentration decreases to 20%. The CoPc@CNT maintains a high FE_{CO} of more than 96% until 50 mA cm^{-2} at the low CO_2 concentration, under which the CoPc+CNT only achieves roughly 20%. The difference trend becomes evident when the CO_2 concentration is turned to 10%, at which CO_2 mass transport plays a more critical role in CO_2RR. Meanwhile, for the single-atom catalyst CoPc@CNT, the partial current densities of CO remain constant despite a 40% to 10% decrease in CO_2 concentration (**Fig. S10**). The CoPc@CNT was subjected to a constant current density test of 100 mA cm^{-2} at different CO_2 concentrations and was compared with bulk Ag and Au catalysts which exhibit excellent CO_2RR performance in CO_2 gas-fed electrolyzers. It turns out that the FE_{CO} of the CoPc@CNT catalyst was maintained at close to 100% when the CO_2 concentration was higher than 10%. In contrast, the bulk Ag catalyst exhibits a significant decline in FE_{CO} as CO_2 concentration drops below 50%, while the bulk Au catalyst' CO_2RR undergoes continuous decay with decreasing CO_2 concentration **(Fig. 2f)**. Meanwhile, the bulk Ag catalyst exhibits a significant decline in CO partial

current densities as the CO_2 concentration decreases, reaching a 50% reduction at -1.7 V with 10% CO_2 **(Fig. S12)**. Therefore, it is confirmed that different from the CoPc+CNT with aggregated CoPc clusters and Ag catalyst with the active sites densely packed on the surface of nanoparticles, CoPc@CNT has uniformly dispersed active sites across the whole carbon matrix, whose stronger CO_2 binding ability enables a higher proportion of CO_2 to exist in the activated form, especially when the CO_2 mass transfer is limited.

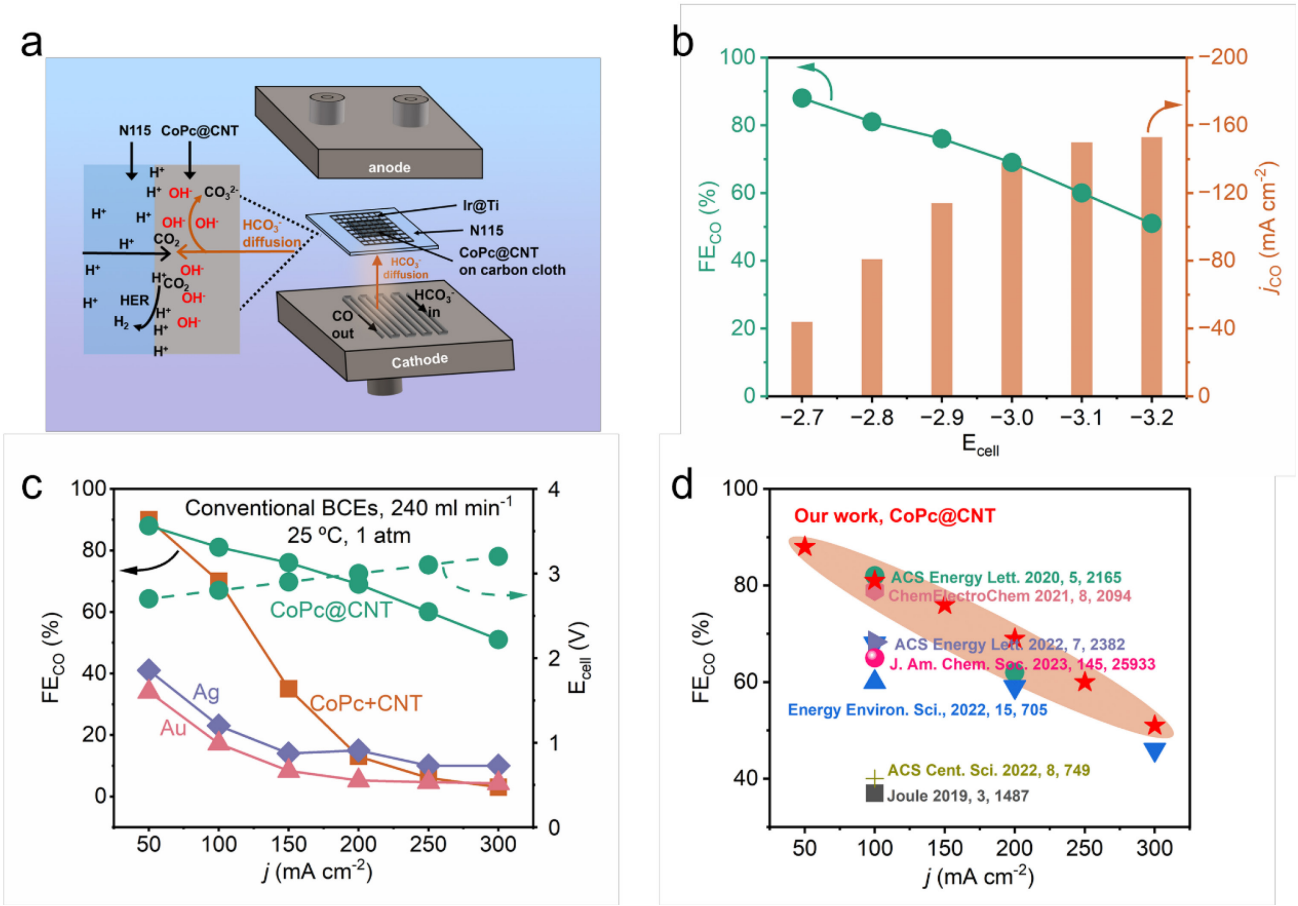

Figure 3: Performance of CoPc@CNT catalyst in conventional BCEs device.

a) Structure of conventional BCEs devices. The cathode catalyst tightly adheres to the proton exchange membrane, with OH^- localized on the catalyst surface, impeding the mass transfer of CO_2. **b**) Partial current density and FE_{CO} of CoPc@CNT at various cell voltages in conventional BCEs devices. **c**) Comparative performance of the FE_{CO} between CoPc@CNT, CoPc+CNT, Ag, and Au catalysts in conventional BCEs devices at different current densities. The right coordinates indicate the E_{cell} of CoPc@CNT at different current densities in conventional BCEs. **d**) Comparison of the FE_{CO} for

CoPc@CNT in conventional BCEs at different current densities with other Ag-based catalysts reported in the literature under room temperature and standard atmospheric pressure.

Molecular Level Strategy for Application in BCEs

To further evaluate the performance of the single-atom catalyst CoPc@CNT in BCEs and confirm the importance of its high CO_2 adsorption capability, we incorporated it into a conventional BCEs device. In this setup, the cathode catalyst layer directly interfaces with the ion exchange membrane, and the bicarbonate solution flows over the back of the porous electrode, where it combines with protons through diffusion to the catalyst surface of the catalyst, resulting in the production of CO_2 (**Fig. 3a**). The CoPc@CNT, prepared with a catalyst loading capacity of 0.6 mg cm^{-2}, was coated onto the porous carbon cloth substrate (**Table S4**). The porous carbon cloth exhibits significant porosity and hydrophilicity (**Fig. S13**), promoting efficient electrolyte flow through the catalyst layer during the reaction. The partial current density of CO experiences a notable increase as the voltage rises from -2.7 V to -3.0 V, reaching a peak of 153 mA cm^{-2} (**Fig. 3b**). Concurrently, the FE_{CO} significantly decreases with more negative voltages, attributed to limited CO_2 mass transfer at higher current densities. Comparison between the performance of CoPc@CNT with CoPc+CNT catalysts containing CoPc clusters, bulk Ag, and Au catalysts reveals interesting insights. At a low current density of 50 mA cm^{-2}, both CoPc@CNT and CoPc+CNT exhibit similar FE_{CO} values exceeding 85% (**Fig. 3c**). However, a substantial disparity emerges as the current density surpasses 100 mA cm^{-2}. At 200 mA cm^{-2}, CoPc@CNT exhibits a remarkable FE_{CO} of 69%, whereas CoPc+CNT only registers 13%. Further amplifying the current density to 300 mA cm^{-2}, CoPc@CNT maintains a FE_{CO} of 51%, while CoPc+CNT plummets to 3%, dominated by the HER. This trend aligns with the results observed in CO_2 gas-fed flow cells with varying CO_2 concentrations (**Fig. 2e**), where CoPc@CNT consistently demonstrates high FE_{CO} across different CO_2 concentrations, while CoPc+CNT exhibits low FE_{CO} at lower CO_2 concentrations. In contrast, for bulk Ag and Au catalysts, the FE_{CO} remains lower even at low current densities due to the weak adsorption capability of CO_2 and decreases as the current densities increase, with the FE_{CO} being below 5% at 300 mA cm^{-2} as well. These findings indicate that the single-atom dispersed catalyst CoPc@CNT effectively enhances CO_2 adsorption and activation in BCEs, owing to its superior CO_2 adsorption capability. Additionally, a performance comparison

between CoPc@CNT and bulk Ag catalysts reported in the literature reveals CoPc@CNT superior FE_{CO} across the range of 50 to 300 mA cm^{-2} (**Fig. 3d**). While the molecular-level strategy to enhance CO_2 adsorption capability proves effective, achieving satisfactory FE_{CO} under high current density requires further system optimization.

Understanding the limitations in CO_2 mass transfer within conventional BCEs devices is crucial for addressing the issue of low faradaic efficiency. At elevated current densities, increased H^+ production from the anode migrates to the cathode. While a surplus of H^+ has the potential to release more CO_2 by reacting with the $KHCO_3$ solution, the inadequate supply of $KHCO_3$ solution from the rear of the catalyst layer results in an accumulation of excess H^+ near the cathode catalyst. This accumulation may inadvertently promote the hydrogen evolution reaction (HER), leading to a reduction in FE_{CO}. Furthermore, under high current density conditions, the increased production of OH^- accumulates on the catalyst surface, forming a CO_2-consuming layer. This layer impedes the mass transfer of CO_2 to the catalyst surface, further diminishing FE_{CO}. Therefore, achieving high FE_{CO} at high current density requires further optimization of the device structure to promote efficient CO_2 mass transfer. This optimization should enhance CO_2 release by fully utilizing H^+ while simultaneously mitigating the presence of OH^- to prevent its consumption of CO_2.

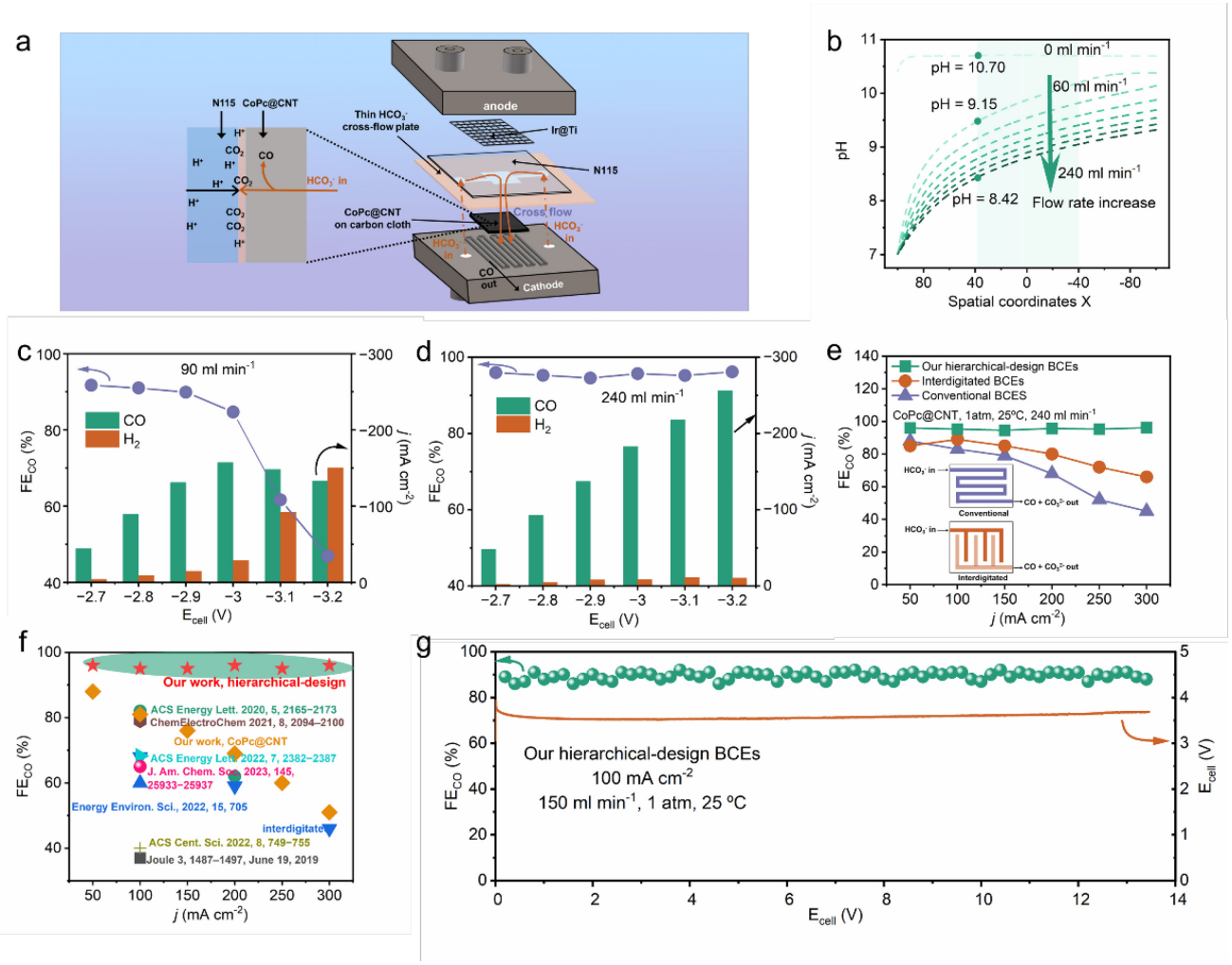

Figure 4: The cross-flow strategy for eliminating the CO_2-consuming layer on the catalyst surface and CO_2RR performance of CoPc@CNT catalyst in the hierarchical design BCEs.

a) The diagram of cathodic electrolytes cross-flow strategy. **b**) COMSOL simulation illustrating the localized pH distribution around the catalyst for different flow rates. Shaded regions indicate the location of the catalyst layer. The value of 0 on the X-axis represents the geometric center spatial position of the catalyst layer. A positive value represents proximity to the anode layer, while a negative value represents proximity to the cathode. **c**), **d**) Partial current density of CO and H_2, and the FE_{CO} as a function of applied electrode potential. **c**) showcase a 90 ml min^{-1} flow rate, while **d**) depict a 240 ml min^{-1} flow rate. **e**) Comparison of performance between various flow plate geometries in conventional BCEs and our hierarchical design BCEs. **f**) Comparison of FE_{CO} achieved in this work with reported literature at varied current densities under room temperature and standard atmospheric pressure. **g**) Stability test of CoPc@CNT catalysts in our hierarchical design BCEs: the catalysts

demonstrate stability for more than 13 hours at a current of 100 mA cm^{-2} and a flow rate of 150 ml min^{-1}.

System Level Strategy to Further Promote CO_2 Mass Transfer

To eliminate the CO_2-consuming layer formed by OH^- on the catalyst surface and enhance CO_2 mass transfer dynamics, the configuration of the cell is crucial. In this regard, a cell configuration has been designed that incorporates a cathodic electrolyte cross-flow between the catalyst layer and the cation exchange membrane (**Fig. 4a**) (**Fig. S14 and Fig. S15**) This cross-flow strategy allows the sufficient supply of HCO_3^- through two special channels directly to the membrane surface, where it combines with H^+ to enhance CO_2 mass transfer. The electrolyte in the cathode chamber then flows out after passing across the cathode electrodes vertically. This cross-flow strategy not only enhances the supply of HCO_3^- and CO_2 but also prevents neutralization by the OH^- generated from the cathodic catalyst (**Eq. S4**), allowing for the optimal utilization of H^+ to release ample CO_2 in situ (**Eq. S2**). Furthermore, the electrolyte flow in the direction from the membrane to the cathode serves the dual purpose of removing OH^- formed on the catalyst surface and transporting CO_2 from the electrolyte bulk to the catalyst surface.

To investigate the impact of the electrolyte cross-flow on CO_2 mass transfer, we constructed a device model and performed COMSOL simulations to calculate the pH around the catalyst layer. As depicted in **Fig. 4b**, the pH value gradually increases from the anode side of the catalyst layer to the back side, confirming that the electrolyte cross flow with the direction from anode to cathode plays an important role in driving OH^- transfer away from the catalyst layer. In the absence of the electrolyte cross flow, the pH on the catalyst surface is as high as 10.7. As the flow rate increases to 240 ml min^{-1}, the pH on the catalyst surface decreases to 8.42, which represents an order of magnitude decrease in the concentration of OH^-. Accordingly, based on the dissolution equilibrium of CO_2 in bicarbonate (**Eq. S6 and Eq. S7**) (**Fig. S16**), theoretical results demonstrated that the CO_2 partial pressure can be significantly increased from 0.11 to 1.14 atm by enhancing the electrolyte cross-flow rate, ensuring sufficient CO_2 supply on the catalyst surface (**Fig. S17**).

To validate the proposed electrolyte cross-flow mechanism, we conducted measurements of the pH

in the single-pass cathodic tailings under various flow rates (**Fig. S18**). To mitigate the buffering effect of bicarbonate that could potentially affect pH accuracy, an alternative K_2SO_4 solution was employed as the electrolyte. Simultaneously, CoPc@CNT served as the cathode catalyst to generate OH^- on the catalyst surface through the hydrogen evolution reaction (HER). The total amount of OH^- remained consistent, regulated by adjusting the current density and reaction time. As depicted in **Fig. S18**, based on the calculated total amount of OH^- and the measured results in the tail bulk solution, the residual OH^- on the catalyst surface gradually decreased by approximately 50% (from 2.3 μmol to 1.2 μmol) as the intensity of the flow rate increased from 60 to 180 ml min^{-1}. This observation demonstrates that the cross-flow strategy effectively removes OH^- from the catalyst surface. It further indicates that the cross-flow strategy eliminates the CO_2-consuming layer and enhances CO_2 mass transfer to the catalyst surface in the BCEs system, aligning with the COMSOL simulation results (**Fig. 4b**).

Building upon the hierarchical strategy outlined, which includes the design of a molecular-level strong CO_2 absorption catalyst and a system-level cross-flow cell, we meticulously evaluated the CO_2RR performance in the new BCEs device. At a low flow rate of 90 ml min^{-1}, the partial current density of CO markedly increases as the voltage rises from -2.7 V to -3.0 V, reaching a maximum of 150 mA cm^{-2} and then slightly decreases. Simultaneously, the FE_{CO} significantly decreases when the voltage is higher than exceeded -3.0 V due to the limited CO_2 mass transfer at high current densities (**Fig. 4c**), which is consistent with the test results in conventional BCEs devices (**Fig. 3b**). Upon increasing the electrolyte flow rate to 240 ml min^{-1}, the partial current densities of CO show a consistent rise with increasing voltage. Especially, the FE_{CO} consistently maintains higher than 96.2% at various voltages (**Fig. 4d**). With increasing flow rates, both the partial current densities and FE_{CO} exhibit improvements, as depicted in **Fig. S19 and Fig. S20**. This trend suggests that the cross-flow of electrolytes effectively eliminates the CO_2-consuming layer on the catalyst surface, facilitating enhanced CO_2 supply.

However, this increased flow rate and subsequent performance enhancement are only effective in our hierarchical-design BCEs, where the mutual coupling of CoPc@CNT and cross-flow strategies is essential. It is found that when CoPc@CNT was used in conventional BCEs, increasing the flow rate did not improve performance, due to the insufficient CO2 supply and OH^- aggregation on the catalyst

surface at high current densities (**Fig. S21**). Comparing the performance of bulk Ag and Au catalysts, or other single-atom catalysts such as NiPc@CNT[37] and FePc@CNT[37,38] in conventional BCEs and cross-flow BCEs, respectively, we found that at the same flow rate, cross-flow strategy did not improve FE_{CO} (**Fig. S22**), which indicates that it is effective only with a catalyst with relatively strong CO_2 adsorption capability, but not excessive, like CoPc@CNT. These comparisons further highlight the innovation of our hierarchical design.

To confirm the effectiveness of our cross-flow BCEs device design, we compared its catalytic performance with those of conventional BCEs device structures featuring serpentine flow plates and optimized interdigitated flow plates (**Fig. 4e**). As expected, our cross-flow BCEs device delivers a 96.2% FE_{CO} under 300 mA cm^{-2}, which is significantly higher than the other two, demonstrating the advantage of our cross-flow BCEs device. Our device achieves the highest FE_{CO} over a wide current range compared with the state-of-the-art BCEs demonstration under room temperature and standard atmospheric pressure (**Fig. 4f**). The hierarchical design BCEs was further tested for stability (**Fig. 4g**), and the FE_{CO} was stable for more than 13 hours at a current density of 100 mA cm^{-2} and a flow rate of 150 ml min^{-1}. XRD and Raman spectra of the catalyst after the reaction showed that the CO_2RR in our hierarchical BCEs did not change the distribution of the catalyst molecules themselves (**Fig. S11**). The decreased stability of the system stemmed from the detachment of the catalyst from the carbon cloth caused by the flow. An effective approach to further improve device stability in future work involves growing the catalyst on the substrate, which prevents the catalyst from being washed away by the high-rate electrolyte flow.

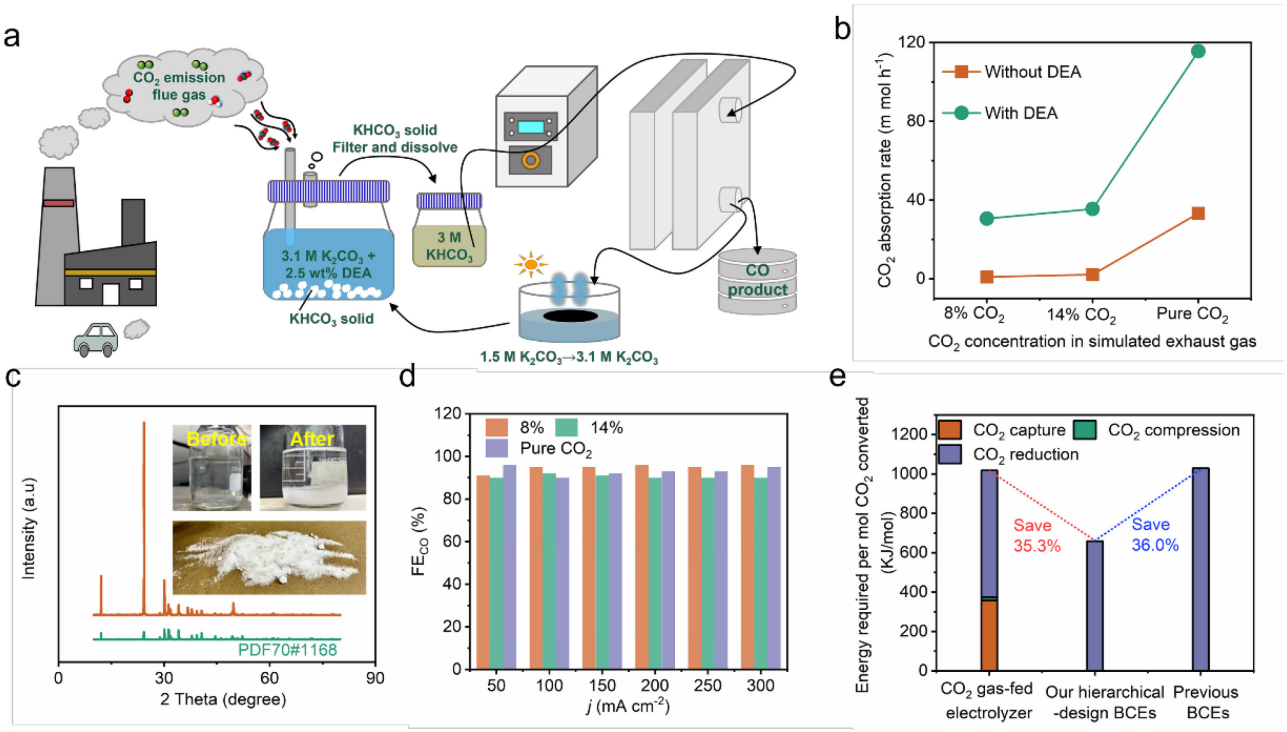

Figure 5: Practical application demonstration of our hierarchical design BCEs.

a) Schematic illustration of CO_2 capture and conversion cycle in BCEs system. **b**) CO_2 capture rate using K_2CO_3 solution for different simulated exhaust gas compositions. **c**) Photograph and XRD analysis of CO_2 capture production by K_2CO_3 solution. **d**) Performance of $KHCO_3$ formed after the capture of CO_2 from different simulated exhaust gas in our hierarchical design BCEs. **e**) Energy consumption comparison between our hierarchical design BCEs and other reported BCEs systems. Energy calculation includes CO_2 capture, compression, and reduction processes. CO_2 conversion efficiency is 50% in CO_2 gas-fed cells and 100% in BCEs.

Practical Application Demonstration

To achieve carbon neutrality in authentic industrial production, it is crucial to design a comprehensive system that integrates CO_2 capture and electrochemical conversion. We have developed a novel, sustainable carbon capture and conversion system based on our hierarchical design BCEs which is suitable to use in industrial exhaust gas with approximately 14% CO_2, as illustrated in **Fig. 5a**. Due to issues such as the low solubility of CO_2 in K_2CO_3 solution and slow reaction rates, the absorption rate of CO_2 by K_2CO_3 solution is relatively slow at room temperature, especially for low concentrations of CO_2 in exhaust gases. The addition of DEA as a promoter can effectively increase

the rate of CO_2 absorption (**Eq. S8-S12**).[39-41] According to proportion based on literature reports and industrial production, 3.1M K_2CO_3 solution containing the 2.5 wt% DEA promoter was employed to capture and convert CO_2 from simulated industrial exhaust gas.[39-41] After electrolysis, $KHCO_3$ was converted to K_2CO_3 which can be used for subsequent CO_2 capture.[13,39,42]

To verify the feasibility of our hierarchical design BCEs linked carbon capture and conversion, we conducted experiments using pure CO_2 and other two simulated exhaust gases which contain a mixture of oxygen and nitrogen and different concentrations of CO_2. **Fig. 5b** illustrates that the CO_2 absorption rate K_2CO_3 solution has a positive correlation to the CO_2 concentration. With DEA introduced, the rate of CO_2 absorption has been accelerated.[43] However, the DEA in BCEs devices poses a challenge to CO_2RR due to its rapid binding to CO_2, resulting in a decline in FE_{CO} (**Fig. S23**). Consequently, we chose to separate $KHCO_3$ from the DEA-containing CO_2 capture solution before it entered the BCEs device. After introducing the simulated exhaust gas into the K_2CO_3 solution for 90 minutes, the initially clear absorption solution gradually became cloudy, accompanied by the formation of white precipitates as depicted in **Fig. 5c**. These white solids were subsequently filtered and characterized via XRD analysis, confirming the generation of $KHCO_3$. Elemental analysis and titration results confirm that the $KHCO_3$ solid produced by capturing CO_2 with K_2CO_3 is of high purity, exceeding 99.9%, and can be directly used for the subsequent conversion in BCEs (**Table S7 and Table S8**). The $KHCO_3$ solids produced from the carbon capture of different CO_2 concentrations nearly have consistent CO_2RR performance in our hierarchical design BCEs (**Fig. 5d**). This demonstrates that our BCEs system has encouraging applicability of different actual exhaust gases with different CO_2 concentrations.

Developing a system that minimizes energy requirements for a fully integrated CO_2 capture and conversion process is challenging. By optimizing the device structure and reducing the thickness of the HCO_3^- flow plate and proton exchange membrane (**Fig. S24**), we achieve energy efficiencies of 35% at 100 mA cm^{-2} and 52% at 10 mA cm^{-2} in BCEs (**Fig. S25**). We counted the total energy cost in our hierarchical design BCEs and compared it to conventional BCEs and conventional gas-fed cells. Due to the significant improvement in FE_{CO} and energy efficiency of our BCEs, energy consumption has been drastically reduced by 36.0% compared to conventional BCEs. Furthermore, Our BCEs system averts the energy-intensive steps such as CO_2 release and compression, resulting in a 35.3%

energy consumption reduction compared to CO_2 gas-fed electrolyzers (**Fig. 5e, Table. S2 and Table. S3**). Therefore, our hierarchically designed BCEs present attractive prospects for practical industrial applications.

DISCUSSION

In summary, our study demonstrates the efficient electrolysis of bicarbonate into CO with faradaic efficiencies reaching 96.2% across the range of 50 to 300 mA cm^{-2}. This success is attributed to a hierarchical design incorporating a single-atom catalyst and a cross-flow cell. Theoretical calculations and electrochemical studies reveal that the single-atom dispersed CoPc@CNT catalyst and electrolyte cross-flow synergistically enhance binding energy interactions with CO_2 and promote CO_2 mass transfer, ensuring an sufficient supply of activated CO_2 for electrochemical reduction. Leveraging the unprecedented FE_{CO}, our hierarchical design BCEs offer significant advantages, including reduced energy consumption, within the integrated CO_2 capture and conversion system. Consequently, this marks a tangible advancement in the practical application of BCEs for efficiently capturing and converting exhaust gas into valuable products.

EXPERIMENTAL PROCEDURES

Resource availability

Lead contact

Further information and requests for resources should be directed to and will be fulfilled by the lead contact, Jia Zhu (jiazhu@nju.edu.cn).

Materials availability

This study did not generate new unique reagents.

Data and code availability

The datasets generated in this study are available from the lead contact on reasonable request.

Materials

All the Chemicals were purchased from commercial sources and used without further purification unless otherwise noted. Ethanol (AR), Nafion solution (5 wt%), Nafion 115 membrane, $KHCO_3$ (AR), and H_2SO_4 (AR) were purchased from commercial suppliers. Ir@Ti mesh electrode (loading: 0.5 mg cm^{-2}, Kunshan

Shengmolong Electrolytic Equipment) was purchased from Kunshan Shengmolong Electrolytic Equipment. Milli-Q water of 18.2 M Ω cm^{-1} was used in all experiments.

Synthesis of CoPc@CNT Single-atom Catalysts

50 mg of CoPc molecules were dispersed in 100 ml of N-N dimethylformamide (DMF) with the assistance of stirring. After removing the insoluble particles from the solution by filtering, a uniformly saturated CoPc solution was obtained. Then, 200 mg of CNTs was added to the above solution and stirred for 7 days to obtain a well-mixed suspension. Subsequently, the mixture was centrifuged and the precipitate was washed with DMF three times and ethanol twice. Finally, the precipitate was lyophilized to yield the final powder of CoPc@CNT.

Cathode Preparation and Electrochemical Measurements

The catalyst ink was prepared as follows. 2 mg of CoPc@CNT powder and 50 μl of 5 wt% Nafion solution were dispersed in 950 μl anhydrous ethanol assisted with ultrasonication for 60 min. Then the catalyst ink was dropped onto carbon cloth (loading 0.6 mg cm^{-2}) as the working electrode. The electrodes in the flow cell were based on hydrophobic carbon paper (29BC) and other factors remained unchanged.

Performance Testing at Different CO_2 Concentrations.

All the performance tests at different CO_2 concentrations of the catalyst were carried out with a three-electrode system in a flow cell. The saturated Ag/AgCl electrode was used as the reference electrode, while an Ir@Ti electrode was used as the counter electrode. The anodic and cathodic electrolytes were 0.5 M $KHCO_3$. All potentials were converted to the reversible hydrogen electrode (RHE) scale using:

$$E(potential, versus\ RHE) = E(versus\ Ag/AgCl) \times 0.197V + 0.0591 \times pH$$

Material Characterizations.

The microscopic structures are characterized by SEM (Tescan, MIRAS3 FE-SEM). Energy dispersive X-ray spectroscopy was performed on FEI Titan G2 60-300. Raman spectra of materials were taken with a home-assembled Raman spectrometer. X-ray diffraction patterns were recorded on D8 Discover (Bruker).

Electrochemical Measurement

Electrochemistry measurements were measured with a two-electrode liquid cross-flow cell system with commercial Ir@Ti as the anode and CoPc@CNT on carbon cloth as the cathode. The geometric areas of the

anode and cathode were 4 cm^2 and 1 cm^2 respectively. Our hierarchical design BCEs were built in-house and consist of housing, gaskets, anode and cathode, an anode proton exchange membrane N115 (3 cm × 3 cm), and a bicarbonate feed plate. The electrolyzer shells were constructed from acrylic sheets. 0.005 M H_2SO_4 (pH = 2) solution was employed as the anolyte for the oxygen evolution reaction and was delivered by a peristaltic pump at 50 mL min^{-1}. The catholyte solution (3.0 M $KHCO_3$) was circulated by a peristaltic pump at a constant flow rate ranging from 90 to 240 ml min^{-1} into the flow-cell electrolyzer, which was then vented back into the flask. The fresh electrolyte was used for each set of experiments. The headspace of the cathode electrolyte reservoir was purged with Ar at 50 sccm throughout each experiment. The gaseous outlet of the catholyte bottle was vented into a gas chromatograph (GC). As references, a conventional cell and an interdigitated cell were also assembled. All the other procedures were the same as those for the cross-flow cell. All the measurements were performed at room temperature (about 25 ° C) and ambient pressure, and three independent experiments were conducted.

Experiments on the Action of Cross-flow Strategy

Electrochemistry measurements were made with a two-electrode liquid cross-flow cell system with commercial Ir@Ti as the anode and CoPc@CNT on carbon cloth as the cathode. The geometric areas of the anode and cathode were 4 cm^2 and 1 cm^2 respectively. The hierarchical design BCEs were built in-house and consisted of housing, gaskets, anode and cathode, an anion exchange membrane FAB-130 (3 cm × 3 cm), and a K_2SO_4 feed plate. The electrolyzer shells were constructed from acrylic sheets. Pure water was employed as the anolyte for the oxygen evolution reaction and was delivered by a peristaltic pump at 50 mL min^{-1}. The catholyte solution (0.1 M K_2SO_4) was circulated by a peristaltic pump at a constant flow rate ranging from 60 to 180 ml min^{-1} into the hierarchical design BCEs, then into the tail-end bulk solution. Measurement of pH using a pH meter. The fresh electrolyte was used for each set of experiments. All the measurements were performed at room temperature (about 25 °C) and ambient pressure, and three independent experiments were conducted.

CO_2 Capture Experiments by K_2CO_3 Solution.

3.1 M K_2CO_3 solution served as the medium for capturing CO_2 from the simulated exhaust gas (8%, 14%, and pure CO_2), and diethanolamine (DEA) was introduced as a catalyst in the solution. Accompanied by carbon capture progress, $KHCO_3$ precipitates were formed and then separated from the DEA-containing solution through filtration. These precipitates were subsequently dissolved in water yielding a fresh 3.0 M $KHCO_3$

solution, which served as the feedstock for the hierarchical design BCEs. After undergoing electrochemical conversion in the hierarchical design BCEs, the regenerative K_2CO_3 solution was 1.5 M and would be concentrated by a photothermal evaporation process to obtain a 3.1 M K_2CO_3 solution, thereby completing the circulation.

DFT Calculation

DFT calculations were performed using the Vienna Ab-Initio Simulation Package (VASP)[44] with the RPBE functional. The core electrons were described with the projector augmented wave (PAW) method.[45] The convergence criteria for electronic and force minimization were set to 10^{-6} eV and 0.02 eV/Å for the structure optimization. The cutoff energy for the kinetic energy of the plane waves was 450 eV. The entropy corrections determined from frequency calculations were performed by using the harmonic oscillator approximation. (3 × 3)-4 layers (111) surfaces were chosen for modeling Ag, where the Brillouin zone was sampled using the (4 × 4 × 1) Gamma-centered k-point grid. For CoPc@CNT, we established a graphene-supported CoPc molecular catalyst model. Only the Γ k-point is sampled.

Grand Canonical DFT calculations (GCDFT) were performed to obtain the potential-dependent energetics, where the number of electrons is allowed to change to adapt to the change of work function along the reaction pathway. The potential-dependent grand canonical free energy can be expressed by a surface charging model:

$$\Omega(U) = \Omega(U) - q(U) \cdot FU \; = \; \Omega(U_0) - \frac{1}{2} C (U - U_0)^2$$

where **Ω**(U) is the electronic energy of the surface at the U potential in SHE scales, q(U) is the charge difference against the neutral condition, and F is the Faradaic constant. C stands for the effective capacitance and U_0 represents the potential of zero charge (pzc). For more details on GCDFT, see our previous work.[46-50] The self-consistent implicit solvation model VASPsol34 is used to represent the polarizable electrolyte region. The dielectric constant 78.3, and the Debye screening length 3 Å, are used, as they correspond to a bulk ion concentration of 1 M.

SUPPLEMENTAL INFORMATION

Supplemental information can be found online at

ACKNOWLEDGMENTS

This work is jointly supported by the National Natural Science Foundation of China (Nos. 92262305, 52302225, 52202251, 51925204), the National Key Research and Development Program of China (No. 2022YFA1404704), Carbon Peaking and Carbon Neutrality Science and Technology Innovation Fund of Jiangsu Province (BK20220035). The authors acknowledge the micro-fabrication center of the National Laboratory of Solid State Microstructures (NLSSM) for technique support. Prof. Jia Zhu acknowledges the support from the XPLORER PRIZE. D.C. and P.S. acknowledged the National Science Foundation CBET Grant 2103116, the Audi CO_2 Cy Pres Award, and Computational resources from the Hoffman2 cluster at UCLA Institute for Digital Research and Education (IDRE). The authors sincerely thank Hua Zhou (Advanced Photon Source, Argonne National Laboratory) for his kind help in measuring X-ray absorption spectroscopy. This research used resources of the Advanced Photon Source (12-BM), a U.S. Department of Energy (DOE) Office of Science User Facility operated for the DOE Office of Science by Argonne National Laboratory under Contract no. DE-AC02-06CH11357.

AUTHOR CONTRIBUTIONS

J.Z. and X.W. conceived the project and designed the experiments. M.S., L.J., Q.X., S.F., S.C., Z.W., and J.W. carried out the synthesis, material characterizations, and electrocatalytic measurements. D.C. and P.S. carried out and analyzed the DFT calculation. Y. L. carried out the COMSOL simulation. M.S. and L.J. analyzed the data and wrote the manuscript. All authors discussed the results and commented on the manuscript.

DECLARATION INTERESTS

The authors declare no competing interests.

References

1. De Luna, P., Hahn, C., Higgins, D., Jaffer, S.A., Jaramillo, T.F., and Sargent, E.H. (2019). What would it take for renewably powered electrosynthesis to displace petrochemical processes? Science *364*, eaav3506. http://doi.org/10.1126/science.aav3506.
2. Li, M., Irtem, E., Iglesias van Montfort, H. P., Abdinejad, M. & Burdyny, T. (2022). Energy comparison of sequential and integrated CO_2 capture and electrochemical conversion. Nat. Commun. *13*, 5398. http://doi.org/10.1038/s41467-022-33145-8.

3. Zhang, Z., Lees, E.W., Habibzadeh, F., Salvatore, D.A., Ren, S., Simpson, G.L., Wheeler, D.G., Liu, A., and Berlinguette, C.P. (2022). Porous metal electrodes enable efficient electrolysis of carbon capture solutions. Energy Environ. Sci. *15*, 705-713. http://doi.org/10.1039/d1ee02608a.
4. Welch, A.J., Dunn, E., DuChene, J.S., and Atwater, H.A. (2020). Bicarbonate or Carbonate Processes for Coupling Carbon Dioxide Capture and Electrochemical Conversion. ACS Energy Lett. *5*, 940-945. http://doi.org/10.1021/acsenergylett.0c00234.
5. Li, M., Yang, K., Abdinejad, M., Zhao, C., and Burdyny, T. (2022). Advancing integrated CO_2 electrochemical conversion with amine-based CO_2 capture: a review. Nanoscale *14*, 11892-11908. http://doi.org/10.1039/d2nr03310k.
6. Xia, Q., Zhang, K., Zheng, T.T., An, L., Xia, C., and Zhang, X. (2023). Integration of CO Capture and Electrochemical Conversion. ACS Energy Lett. *8*, 2840-2857. http://doi.org/10.1021/acsenergylett.3c00738.
7. Zhang, Z., Lees, E.W., Ren, S., Mowbray, B.A.W., Huang, A., and Berlinguette, C.P. (2022). Conversion of Reactive Carbon Solutions into CO at Low Voltage and High Carbon Efficiency. ACS Cent. Sci. *8*, 749-755. http://doi.org/10.1021/acscentsci.2c00329.
8. Kim, J., Guo, W., Kim, H., Choe, S., Kim, S.Y., and Ahn, S.H. (2022). Gaseous CO_2 Electrolysis: Progress, Challenges, and Prospects. ACS Sustainable Chem. Eng. *10*, 14092-14111. http://doi.org/10.1021/acssuschemeng.2c04501.
9. Salvatore, D., and Berlinguette, C.P. (2019). Voltage Matters When Reducing CO_2 in an Electrochemical Flow Cell. ACS Energy Lett. *5*, 215-220. http://doi.org/10.1021/acsenergylett.9b02356.
10. Verma, S., Kim, B., Jhong, H.R.M., Ma, S., and Kenis, P.J.A. (2016). A Gross-Margin Model for Defining Technoeconomic Benchmarks in the Electroreduction of CO_2. ChemSusChem *9*, 1972-1979. http://doi.org/10.1002/cssc.201600394.
11. Fink, A.G., Lees, E.W., Zhang, Z.S., Ren, S.X., Delima, R.S., and Berlinguette, C.P. (2021). Impact of Alkali Cation Identity on the Conversion of HCO_3^- to CO in Bicarbonate Electrolyzers. Chemelectrochem *8*, 2094-2100. http://doi.org/10.1002/celc.202100408.
12. Zhang, Z., Melo, L., Jansonius, R.P., Habibzadeh, F., Grant, E.R., and Berlinguette, C.P. (2020). pH Matters When Reducing CO_2 in an Electrochemical Flow Cell. ACS Energy Lett. *5*, 3101-3107. http://doi.org/10.1021/acsenergylett.0c01606.
13. Kar, S., Rahaman, M., Andrei, V., Bhattacharjee, S., Roy, S., and Reisner, E. (2023). Integrated capture and solar-driven utilization of CO_2 from flue gas and air. Joule *7*, 1496-1514. http://doi.org/10.1016/j.joule.2023.05.022.
14. Lee, G., Li, Y.C., Kim, J.-Y., Peng, T., Nam, D.-H., Sedighian Rasouli, A., Li, F., Luo, M., Ip, A.H., Joo, Y.-C., and Sargent, E.H. (2020). Electrochemical upgrade of CO_2 from amine capture solution. Nat. Energy *6*, 46-53. http://doi.org/10.1038/s41560-020-00735-z.
15. Liu, H., Chen, Y., Lee, J., Gu, S., and Li, W. (2022). Ammonia-Mediated CO_2 Capture and Direct Electroreduction to Formate. ACS Energy Lett. *7*, 4483-4489. http://doi.org/10.1021/acsenergylett.2c02247.
16. Li, H.Y., Gao, J.M., Du, Q., Shan, J.J., Zhang, Y., Wu, S.H., and Wang, Z.J. (2021). Direct CO_2 electroreduction from NH_4HCO_3 electrolyte to syngas on bromine-modified Ag catalyst. Energy *216*, 119250. http://doi.org/10.1016/j.energy.2020.119250
10.1016/j.energy.2020.119250.
17. Gutiérrez-Sánchez, O., de Mot, B., Daems, N., Bulut, M., Vaes, J., Pant, D., and Breugelmans, T. (2022). Electrochemical Conversion of CO_2 from Direct Air Capture Solutions. Energy Fuels *36*, 13115-13123.

http://doi.org/10.1021/acs.energyfuels.2c02623.

18. Li, Y.C., Lee, G., Yuan, T., Wang, Y., Nam, D.-H., Wang, Z., García de Arquer, F.P., Lum, Y., Dinh, C.-T., Voznyy, O., and Sargent, E.H. (2019). CO_2 Electroreduction from Carbonate Electrolyte. ACS Energy Lett. *4*, 1427-1431. http://doi.org/10.1021/acsenergylett.9b00975.
19. Lees, E.W., Goldman, M., Fink, A.G., Dvorak, D.J., Salvatore, D.A., Zhang, Z., Loo, N.W.X., and Berlinguette, C.P. (2020). Electrodes Designed for Converting Bicarbonate into CO. ACS Energy Lett. *5*, 2165-2173. http://doi.org/10.1021/acsenergylett.0c00898.
20. Kim, Y., Lees, E.W., and Berlinguette, C.P. (2022). Permeability Matters When Reducing CO_2 in an Electrochemical Flow Cell. ACS Energy Lett. *7*, 2382-2387. http://doi.org/10.1021/acsenergylett.2c01160.
21. Li, T., Lees, E.W., Goldman, M., Salvatore, D.A., Weekes, D.M., and Berlinguette, C.P. (2019). Electrolytic Conversion of Bicarbonate into CO in a Flow Cell. Joule *3*, 1487-1497. http://doi.org/10.1016/j.joule.2019.05.021.
22. Alvarez, A., Borges, M., Corral-Perez, J.J., Olcina, J.G., Hu, L., Cornu, D., Huang, R., Stoian, D., and Urakawa, A. (2017). CO_2 Activation over Catalytic Surfaces. Chemphyschem *18*, 3135-3141. http://doi.org/10.1002/cphc.201700782.
23. Jin, S., Hao, Z., Zhang, K., Yan, Z., and Chen, J. (2021). Advances and Challenges for the Electrochemical Reduction of CO_2 to CO: From Fundamentals to Industrialization. Angew. Chem., Int. Ed. Engl. *60*, 20627-20648. http://doi.org/10.1002/anie.202101818.
24. Nitopi, S., Bertheussen, E., Scott, S.B., Liu, X., Engstfeld, A.K., Horch, S., Seger, B., Stephens, I.E.L., Chan, K., Hahn, C., et al. (2019). Progress and Perspectives of Electrochemical CO_2 Reduction on Copper in Aqueous Electrolyte. Chem. Rev. *119*, 7610-7672. http://doi.org/10.1021/acs.chemrev.8b00705.
25. Feng, S., Wang, X., Cheng, D., Luo, Y., Shen, M., Wang, J., Zhao, W., Fang, S., Zheng, H., Ji, L., et al. (2024). Stabilizing *CO_2 Intermediates at the Acidic Interface using Molecularly Dispersed Cobalt Phthalocyanine as Catalysts for CO_2 Reduction. Angew. Chem., Int. Ed. Engl., e202317942. http://doi.org/10.1002/anie.202317942.
26. Birdja, Y.Y., Pérez-Gallent, E., Figueiredo, M.C., Göttle, A.J., Calle-Vallejo, F., and Koper, M.T.M. (2019). Advances and challenges in understanding the electrocatalytic conversion of carbon dioxide to fuels. Nat. Energy *4*, 732-745. http://doi.org/10.1038/s41560-019-0450-y.
27. Kim, D., Choi, W., Lee, H.W., Lee, S.Y., Choi, Y., Lee, D.K., Kim, W., Na, J., Lee, U., Hwang, Y.J., and Won, D.H. (2021). Electrocatalytic Reduction of Low Concentrations of CO_2 Gas in a Membrane Electrode Assembly Electrolyzer. ACS Energy Lett. *6*, 3488-3495. http://doi.org/10.1021/acsenergylett.1c01797.
28. Fu, J., Zhu, L., Jiang, K., Liu, K., Wang, Z., Qiu, X., Li, H., Hu, J., Pan, H., Lu, Y.-R., et al. (2021). Activation of CO_2 on graphitic carbon nitride supported single-atom cobalt sites. Chem. Eng. J. *415*, 128982. http://doi.org/10.1016/j.cej.2021.128982.
29. Chen, J.M., Xie, W.J., Yang, Z.W., and He, L.N. (2022). Cobalt Phthalocyanine Cross-Linked Polypyrrole for Efficient Electroreduction of Low Concentration CO_2 To CO. ChemSusChem *15*, e202201455. http://doi.org/10.1002/cssc.202201455.
30. Nørskov, J.K., Studt, F., Abild-Pedersen, F., and Bligaard, T. (2014). Fundamental Concepts in Heterogeneous Catalysis. Fundamental Concepts in Heterogeneous Catalysis, John Wiley & Sons, Inc.,New Jersey, 79-84. http://doi.org/10.1002/9781118892114.
31. Ren, S., Joulie, D., Salvatore, D., Torbensen, K., Wang, M., Robert, M., and Berlinguette, C.P. (2019).

Molecular electrocatalysts can mediate fast, selective CO_2 reduction in a flow cell. Science *365*, 367-369. http://doi.org/10.1126/science.aax4608.

32. Wu, Y., Jiang, Z., Lu, X., Liang, Y., and Wang, H. (2019). Domino electroreduction of CO_2 to methanol on a molecular catalyst. Nature *575*, 639-642. http://doi.org/10.1038/s41586-019-1760-8.
33. Nam, D.H., De Luna, P., Rosas-Hernandez, A., Thevenon, A., Li, F., Agapie, T., Peters, J.C., Shekhah, O., Eddaoudi, M., and Sargent, E.H. (2020). Molecular enhancement of heterogeneous CO_2 reduction. Nat. Mater. *19*, 266-276. http://doi.org/10.1038/s41563-020-0610-2.
34. Su, J., Musgrave, C.B., Song, Y., Huang, L., Liu, Y., Li, G., Xin, Y., Xiong, P., Li, M.M.-J., Wu, H., et al. (2023). Strain enhances the activity of molecular electrocatalysts via carbon nanotube supports. Nat. Catal. *6*, 818-828. http://doi.org/10.1038/s41929-023-01005-3.
35. Zhang, X., Wu, Z., Zhang, X., Li, L., Li, Y., Xu, H., Li, X., Yu, X., Zhang, Z., Liang, Y., and Wang, H. (2017). Highly selective and active CO_2 reduction electrocatalysts based on cobalt phthalocyanine/carbon nanotube hybrid structures. Nat. Commun. *8*, 14675. http://doi.org/10.1038/ncomms14675.
36. Vijay, S., Ju, W., Brückner, S., Tsang, S.-C., Strasser, P., and Chan, K. (2021). Unified mechanistic understanding of CO_2 reduction to CO on transition metal and single atom catalysts. Nature Catal. *4*, 1024-1031. http://doi.org/10.1038/s41929-021-00705-y.
37. Wang, Y., Jiang, Z., Zhang, X., Niu, Z., Zhou, Q., Wang, X., Li, H., Lin, Z., Zheng, H., and Liang, Y. (2020). Metal Phthalocyanine-Derived Single-Atom Catalysts for Selective CO_2 Electroreduction under High Current Densities. ACS Appl. Mater. Interfaces *12*, 33795-33802. http://doi.org/10.1021/acsami.0c08940.
38. Zeng, Y., Zhao, J., Wang, S., Ren, X., Tan, Y., Lu, Y.-R., Xi, S., Wang, J., Jaouen, F., Li, X., et al. (2023). Unraveling the Electronic Structure and Dynamics of the Atomically Dispersed Iron Sites in Electrochemical CO_2 Reduction. J. Am. Chem. Soc. *145*, 15600-15610. http://doi.org/10.1021/jacs.3c05457.
39. Hu, G., Nicholas, N.J., Smith, K.H., Mumford, K.A., Kentish, S.E., and Stevens, G.W. (2016). Carbon dioxide absorption into promoted potassium carbonate solutions: A review. Int. J. Greenhouse Gas Control *53*, 28-40. http://doi.org/10.1016/j.ijggc.2016.07.020.
40. Ramazani, R., Mazinani, S., Jahanmiri, A., and Van der Bruggen, B. (2016). Experimental investigation of the effect of addition of different activators to aqueous solution of potassium carbonate: Absorption rate and solubility. Int. J. Greenhouse Gas Control *45*, 27-33. http://doi.org/10.1016/j.ijggc.2015.12.003.
41. Borhani, T.N.G., Akbari, V., Afkhamipour, M., Hamid, M.K.A., and Manan, Z.A. (2015). Comparison of equilibrium and non-equilibrium models of a tray column for post-combustion CO_2 capture using DEA-promoted potassium carbonate solution. Chem. Eng. Sci. *122*, 291-298. http://doi.org/10.1016/j.ces.2014.09.017.
42. Liu, H., Li, M., Luo, X., Liang, Z., Idem, R., and Tontiwachwuthikul, P. (2018). Investigation mechanism of DEA as an activator on aqueous MEA solution for postcombustion CO_2 capture. AIChE J. *64*, 2515-2525. http://doi.org/10.1002/aic.16165.
43. Kim, Y., Lees, E.W., Donde, C., Waizenegger, C.E.B., Simpson, G.L., Valji, A., and Berlinguette, C.P. (2023). Electrochemical capture and conversion of CO_2 into syngas. ChemRxiv. *1*. http://doi.org/10.26434/chemrxiv-2023-hvjxn.
44. Kresse, G., and Furthmuller, J. (1996). Efficiency of ab-initio total energy calculations for metals and semiconductors using a plane-wave basis set. Comput. Mater. Sci. *6*, 15-50. http://doi.org/10.1016/0927-0256(96)00008-0.

45. Kresse, G., and Joubert, D. (1999). From ultrasoft pseudopotentials to the projector augmented-wave method. Phys. Rev. B *59*, 1758-1775. http://doi.org/10.1103/PhysRevB.59.1758.
46. Cheng, D., Wei, Z., Zhang, Z., Broekmann, P., Alexandrova, A.N., and Sautet, P. (2023). Restructuring and Activation of Cu(111) under Electrocatalytic Reduction Conditions. Angew. Chem., Int. Ed. Engl. *62*, e202218575. http://doi.org/10.1002/anie.202218575.
47. Steinmann, S.N., Michel, C., Schwiedernoch, R., and Sautet, P. (2015). Impacts of electrode potentials and solvents on the electroreduction of CO_2: a comparison of theoretical approaches. Phys. Chem. Chem. Phys. *17*, 13949-13963. http://doi.org/10.1039/c5cp00946d.
48. Steinmann, S.N., Sautet, P., and Michel, C. (2016). Solvation free energies for periodic surfaces: comparison of implicit and explicit solvation models. Phys. Chem. Chem. Phys. *18*, 31850-31861. http://doi.org/10.1039/c6cp04094b.
49. Wei, Z., Goltl, F., Steinmann, S.N., and Sautet, P. (2022). Modeling Electrochemical Processes with Grand Canonical Treatment of Many-Body Perturbation Theory. J. Phys. Chem. Lett. *13*, 6079-6084. http://doi.org/10.1021/acs.jpclett.2c01376.
50. Mathew, K., Kolluru, V.S.C., Mula, S., Steinmann, S.N., and Hennig, R.G. (2019). Implicit self-consistent electrolyte model in plane-wave density-functional theory. J. Chem. Phys. *151*, 234101. http://doi.org/10.1063/1.5132354.